1 Unexpected land-surface warming following a low-to-moderate
2 forcing hypothetical nuclear war

3 Anson Ka Hei Cheung[1], Paul J. Kushner[1], Francesco S. R. Pausata[2], Zhihong Zhuo[2], Marguerite
4 L. Brown[2]

5 [1]Department of Physics, University of Toronto

6 [2]Department of Earth and Atmospheric Sciences, University of Quebec in Montreal
7 *Correspondence to*: Anson Ka Hei Cheung (anson.cheung@mail.utoronto.ca), Paul J. Kushner
8 (paul.kushner@utoronto.ca)

9 **Abstract.** Nuclear conflicts could ignite intense urban fires that inject considerable amounts of black carbon (BC)

10 into the upper atmosphere, with the potential to disrupt global climate. While uncertainties in the total BC injection

11 remain large, relatively few modeling studies and limited model diversity have explored the climatic response to

12 low-to-moderate BC injections, leaving key aspects of their climate impact poorly understood. Here, we investigate

13 the climate response to a set of low-to-moderate forcing scenarios (12 to 24 Tg BC) – roughly one-tenth to one-fifth

14 the strength of the standard high-end cases – using the Canadian Earth System Model version 5. Consistent with

15 previous work, we find prolonged global reductions in surface temperature and precipitation, driven by decreased

16 downwelling shortwave radiation at the surface and increased atmospheric stability. Unexpectedly, however, a

17 transient surface warming develops in the first boreal summer following a boreal-winter injection, linked to reduced

18 net longwave and turbulent fluxes. Precipitation remains suppressed because of enhanced stability. The transient

19 warming is most pronounced for the lowest forcing cases, indicating a nonlinear response across the forcing range.

20 These results underscore the need for broader multi-model assessments and systematic exploration across a wider

21 range of scenarios, given their potential for complex, societally relevant outcomes.

22 1 Introduction

23 Although the global nuclear arsenal has shrunk since the Cold War, global society is still threatened by potential

24 nuclear conflict due to rising geopolitical tension and the proliferation of regional nuclear powers. In addition to local

25 damage and health effects at the locations of nuclear detonation (Lucas et al., 1990; Solomon & Marston, 1986),

26 regional nuclear conflicts can have global climatic effects, including stratospheric warming, surface cooling, and

27 reduced precipitation (Coupe et al., 2019; Robock et al., 2007a; Toon et al., 2007) as well as reduction in the ozone

28 layer thickness (Mills et al., 2008; Mills et al., 2014).

29 The global effects stem from firestorms that are triggered at targeted urban and industrial centers. The firestorms can

30 induce convection capable of injecting a great amount of inorganic and organic carbon into the upper troposphere -

31 lower stratosphere (UTLS) (Tarshish & Romps, 2022; Toon et al., 2007). Climate modeling studies have shown that

32 the carbonaceous aerosol can heat the upper atmosphere and cool the Earth's surface by increasing the absorption of

33 solar radiation aloft (Pausata et al., 2016; Robock et al., 2007a). Upon local heating, the aerosol-laden air becomes

34 buoyant and rises to a higher altitude. This 'self-lofting' prolongs the aerosol residence time (Johnson & Haywood,

35   2023; Malone et al., 1985; Ohneiser et al., 2023). In a hypothetical case of a full-scale nuclear exchange between the
36   United States and Russia, a UTLS injection of a large amount of black carbon (BC) would drive unprecedented
37   stratospheric warming and surface cooling at a global scale (Robock et al., 2007a). The surface cooling may lead to
38   crop failure and famine, slowing down societal recovery (Xia & Robock, 2013; Xia et al., 2015, Xia et al., 2022).
39   Precipitation would also be reduced globally due to reduction in solar heating, evaporation, and convection. Disruption
40   of stratospheric chemistry would lead to ozone depletion via various mechanisms even for a modest BC injection in a
41   nuclear conflict between India and Pakistan (Mills et al., 2008; Mills et al., 2014). The resulting increase in surface
42   UV radiation could damage human health and ecosystems on a global scale.

43   Both the amounts of BC emission and UTLS injection are highly uncertain. Taking into account the uncertainties in
44   the BC-emission factors of flammable materials and the quantities to be burned, Turco et al. (1990) considered a wide
45   range of plausible BC emissions, from 20 to 290 Tg, that could arise as a result of a full-scale nuclear exchange
46   involving the North Atlantic Treaty Organization (NATO) and Warsaw Pact nations. Beside emission factor uncertainty,
47   variations in local meteorology, modern warfare tactics, and rubblization of fuels all contribute to the uncertainty in
48   the total amount of BC injected into UTLS (Glasstone & Dolan, 1977; NASEM, 2025; Tarshish & Romps, 2022).
49   However, for this full-scale nuclear exchange scenario, most studies considered a UTLS injection of 150 Tg BC as a
50   standard scenario (Bardeen et al., 2021; Coupe et al., 2019; Robock et al., 2007a), with little attention given to low-
51   to-moderate forcing scenarios involving smaller BC injections from nuclear-war fires. Yet a nuclear conflict would
52   not necessarily entail the use of the entire arsenal; assessing the climate effects of such partial or regional exchanges
53   is therefore essential to capture the plausible range of outcomes. In this context, smaller injection estimates on the
54   order of 10-25 Tg BC become particularly relevant, as they represent plausible outcomes of limited nuclear exchanges
55   rather than full-scale global war. For instance, a UTLS injection of 10-25 Tg BC for the USA-Russia scenario would
56   be small compared to the 150 Tg load in Coupe et al. (2019) and Robock et al. (2007a) but still extreme relative to
57   natural forcing or recent forest fires. For comparison, the 2019 Australian wildfires emitted 0.9 Tg of smoke into the
58   stratosphere, of which 2.5% was BC and the remainder mostly organic carbon (OC) (Yu et al., 2021). Model
59   calculations estimated a statistically significant warming and ozone depletion in the southern hemispheric midlatitude
60   stratosphere for 6 months as a result of these wildfire emissions. Compared to typical wildfires, the smoke injected
61   into the UTLS would have a higher BC-to-OC ratio due to lower oxygen content in large-scale urban fires (Shemwell
62   & Levendis, 2000; Tewarson, 2002; Toon et al., 2007). Therefore, it is a pertinent question to ask how the climate
63   response might differ under a low-to-moderate BC injection scenario.

64   In this study, we look into the climate response to relatively weak BC injection with the use of an atmosphere-ocean
65   coupled model, the Canadian Earth System Model version 5.1 (CanESM5; Swart et al., 2019). This is the first time
66   CanESM is used for the study of nuclear war fire emissions. Its independent development from other climate models
67   helps characterize model uncertainty. Although it is a low top model with a coarse stratospheric representation and a
68   lack of stratospheric chemistry and aerosol model, it is a workhorse ESM that has been extensively used in many
69   climate simulations studying anthropogenic climate change effects stemming from the Coupled Model
70   Intercomparison Project phase 6 (CMIP6; Eyring et al., 2016, Samset et al., 2025). We test the sensitivity of the

71   response by varying the total BC injection around the low end of the estimated emission in a full-scale nuclear

72   exchange, between 12 and 24 Tg. This study represents an effort to investigate this model's climate response to such

73   forcing before the CanESM system moves to subsequent more advanced versions with updates to the aerosol scheme.

74   In this study, we find a previously undocumented transient 'whiplash' as the model transitions to a nuclear winter state

75   through an early summertime warming response, unexpectedly strong high-latitude responses to stratospheric BC

76   injection, and other effects. This relatively weak but plausible forcing scenario bears investigating in other models.

77   In Section 2, we provide a description of the model used and parameterizations of relevant processes, as well as the

78   experimental set-up. In Section 3, we investigate the climate response to different amounts of BC emission in the low-

79   to-moderate forcing scenarios. In Section 4, we summarize the results and discuss the potential implications and future

80   work.

81   **2 Methods**

82   **2.1 Model description**

83   We conduct the simulations using the Canadian Earth System Model version 5.1 (CanESM5; Swart et al., 2019), which

84   contains an atmosphere component that incorporates a land model, coupled with the ocean model NEMO (Madec &

85   the NEMO team, 2012). The atmosphere component of CanESM5 is the Canadian Atmospheric Model version 5

86   (CanAM5) with a bulk aerosol scheme employed (Cole et al., 2023). It is a T63 spectral dynamical core model (2.8°

87   horizontal resolution) with 49 vertical layers with layer thickness that increases monotonically from approximately

88   100 m at the surface to 2 km at about 1 hPa, which is the upper bound. The number of vertical levels has been increased

89   from its predecessor, CanAM4 (von Salzen et al., 2013), to match those employed by the Canadian Middle Atmosphere

90   Model (Scinocca et al., 2008), but the stratosphere is still coarsely represented, with 18 levels from about 300 hPa to

91   10 hPa. The quasi-biennial oscillation is not simulated by CanAM5. Biases in stratospheric temperature and zonal

92   wind are reduced in CanAM5 relative to CanAM4 (Cole et al., 2023). Despite having a low model top, CanESM5 has

93   been used in the framework of understanding climate perturbations involving dynamical and radiative coupling of the

94   troposphere to the lower stratosphere. For example, it has been used in the Model Intercomparison Project on the

95   climatic response to volcanic forcing (VolMIP; Zanchettin et al., 2016), which is an endorsed contribution to the

96   CMIP6. It also has good performance in realizing the Arctic sea-level pressure response to sudden stratospheric

97   warming among CMIP6 models when compared to reanalysis (Dai et al., 2024), suggesting that it simulates

98   stratosphere-troposphere interactions adequately for our sensitivity study.

99   CanAM5 employs bulk cloud microphysical parameterizations that depend on the mean water content and other

100 moments of droplet size distributions (von Salzen et al., 2013). The autoconversion, cloud liquid water content, and

101 cloud lifetime depend on a cloud droplet number concentration that is a function of sulphate concentration (Ghan et

102 al., 2013; Wood, 2005). The latter parameterization represents what is known as the second aerosol indirect effect.

103 CanAM5 also parameterizes the BC semi-direct radiative effect as a perturbation to existing liquid cloud optical

104 properties according to the volume fraction of BC to cloud water (Li et al., 2013). The cloud processes are limited to

105   pressures greater than 10 hPa given the uncertainty in the applicability of the parameterizations at high altitudes.

106   Aerosols that are considered in CanAM5 include sulfate, BC, OC, sea salt, and mineral dust. Hydrophilic BC,

107   hydrophilic OC, and sulfate are assumed to be internally mixed in CanAM5 and have a refractive index that depends

108   on the fraction, effective radius, and effective variance of each component aerosol, as well as the relative humidity

109   (Wu et al., 2018). CanAM5 does not take into account the aerosol number for determining gravitational settling rate,

110   unlike some other models that have been used for the climate impact study of nuclear conflicts such as NorESM1-M

111   (Pausata et al., 2016) and CESM2-WACCM6 (Gettelman et al., 2019).

112   Aerosols are removed from the atmosphere by dry and wet deposition. In CanAM5, the dry deposition flux is

113   parameterized based on near-surface aerosol concentration and a specified dry deposition velocity that depends on the

114   type of tracer and the local surface condition (Croft et al., 2005; Lohmann et al., 1999). For wet deposition, CanAM5

115   includes below-cloud scavenging for stratiform clouds and in-cloud scavenging for both stratiform and convective

116   clouds. The below-cloud scavenging rate depends on the precipitation rate, whereas the in-cloud scavenging rates

117   depend on the precipitation formation rate. The snow-darkening effect of BC deposition is also included in CanAM5.

118   The total BC deposition flux is used to calculate the BC mass budget in snow layer, whose snow albedo is

119   parameterized as a function of BC mass mixing ratio in snow, snow water equivalent, snow grain size, underlying

120   surface albedo, and solar zenith angle (Namazi, et al., 2015).

121   **2.2 Experimental design**

122   We generate an ensemble with an injection of 20 Tg of BC (hereafter as BC20), consisting of 15 ensemble members.

123   To generate the ensemble members, we select different years from a 100-year pre-industrial control simulation as the

124   initial years (Eyring et al., 2016). All selected years are at a neutral state of the El Niño-Southern Oscillation (ENSO)

125   in January to avoid potential ENSO imprint on the simulated responses. To test the sensitivity of the global mean

126   climate response to BC aerosol, we generate 3 additional ensembles, each consisting of 3 ensemble members, with an

127   injection of 12 Tg, 16 Tg, and 24 Tg of BC (hereafter as BC12, BC16, and BC24), respectively. While we were

128   interested in extending beyond this limit, we have found that the model was rendered unstable for forcings greater

129   than about 40 Tg and that the climate response exhibits unexpected features even in the low-to-moderate forcing

130   scenarios. All injected BC particles are assumed hydrophilic from the start. As in previous studies, the particles are

131   injected uniformly between 300 to 150 hPa over the United States and Russia at a constant rate over 1 week, starting

132   from January 1st. To evaluate the long-term response, each simulation is run for 20 years from the first day of emission.

133   **3 Results**

134   **3.1 BC burden response and impacts on global shortwave and longwave radiation**

135   For all cases, more than two-thirds of the BC burden stays under the overworld, which is defined as the domain above

136   the 380 K potential temperature surface (around 15 km above the Earth's surface) (Holton et al., 1995), and gets

137   removed in the first year (Fig. 1a). The BC burden in the lower atmosphere (under the 380 K potential temperature

138   surface) is relatively greater in the first year before getting removed, which is important for the shorter-term climate

139 response. The overworld burden for BC12 attains its maximum at 2.0 Tg in first year June, while the overworld burden

140 for BC24 attains its maximum at 5.2 Tg in the same month, so doubling the injection from 12 Tg to 24 Tg results in

141 more than 2.5 times more BC being lofted into the overworld. After reaching the maximum burden in the overworld,

142 the overworld BC mass e-folding time, which is defined by the time it takes for the burden to reach e^{-1} of its maximum,

143 for BC16, BC20, and BC24 is estimated between 3 years and 6 months, and 3 years and 8 months, while the mass e-

144 folding time for BC12 is 3 years and 3 months. In the lower atmosphere, the mass e-folding time is 3 months for all 4

145 cases. Throughout the simulated period, the fraction of remaining mass of BC is greater in the larger-forcing scenario

146 (Fig. 1b). The nonlinear dependence of early-stage BC lofting on the total mass of injection influences the long-term

147 climate response since the overworld burden has a much longer residence time compared to lower atmospheric burden.

148
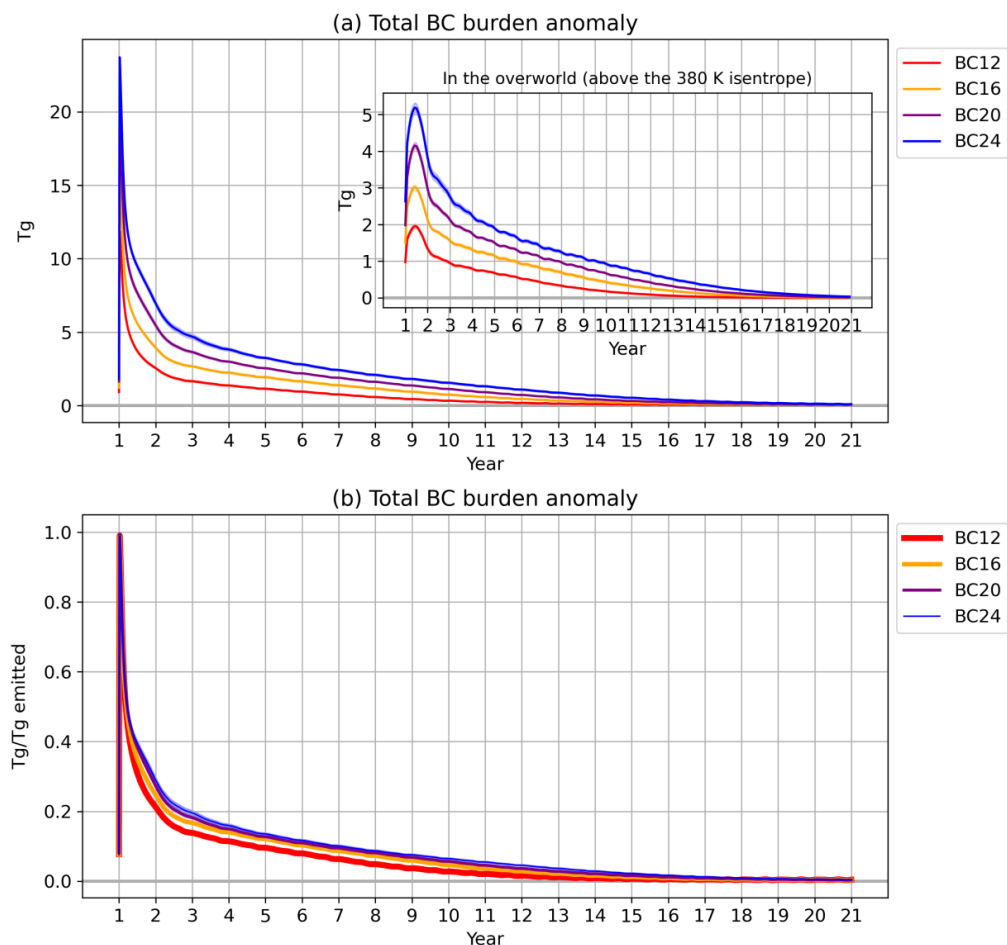
Figure 1. Daily averaged BC burden anomalies relative to the control simulation (a) in the atmosphere, (inset of a) in the overworld domain, and (b) in the atmosphere per Tg of emitted BC. Shading indicates the standard error of the mean. In (b), the lines for different ensembles are varied in thickness to show where they overlap.

As will be shown, the climate responses exhibit distinct behaviours during January to February (JF) of first year, June to August (JJA) of first year, and years 6 to 15. The temporal means of the climate responses for these primary periods of interest will be highlighted throughout this section (Table 1).

Absorption of solar radiation by BC reduces surface downwelling shortwave radiative flux (DSRF). The response in the global mean surface DSRF reaches a minimum in two months following the UTLS injection BC (Fig. 2a). The response is -14.80 W m^{-2} and -26.96 W m^{-2} in first year January and February for BC12 and BC24, respectively (Table

160 1). As the BC aerosol is removed from the atmosphere, the response gradually diminishes. The reduction in the global
161 mean DSRF per unit mass of burden has not been maximized in the first two months when the global mean DSRF
162 reduction reaches the maximum since the BC aerosol is still concentrated in the Northern Hemisphere (NH) (Fig. 2a
163 inset and see description of Fig. 3a on BC interhemispheric transport). The efficiency of reduction is maximized in
164 July of the first year as the BC is transported globally (see below). Doubling the BC injection from 12 to 24 Tg causes
165 the reduction per Tg burden to decrease from –3.63 to –2.91 W m^{-2} Tg^{-1} in first year JJA (Table 1). After the first year,
166 the surface DSRF reduction per Tg burden is comparable across all the cases. This indicates approximately a linear
167 scaling of the surface DSRF reduction with the atmospheric burden of BC, which is expected for low-to-moderate
168 forcing scenarios. Although the surface DSRF reduction per Tg burden is comparable across the scenarios, the BC
169 burden decreases at a faster rate for the weaker forcing scenarios (Fig. 1b), resulting in a smaller surface DSRF
170 reduction per Tg injection in the long term (Table 1). Comparing BC12 and BC24, the surface DSRF reduction per Tg
171 injection for BC12 is initially comparable to that for BC24 but becomes only about half of the value for BC24 in years
172 6 to 15 (Table 1). This implies that by allowing more BC aerosol to reach the overworld, the stronger early-stage self-
173 lofting effect in BC24 contributes to the reduction of DSRF at the surface in the long term. This translates to a nonlinear
174 response in the long-term surface temperature response, as will be shown below.

175

	DSRF	DSRF per Tg burden	DSRF per Tg injection	DLRF	DLRF per Tg burden	DLRF per Tg injection	TS	TS per Tg burden	TS per Tg injection
First year JF	-26.96 ± 2.38 (-14.80 ± 1.29)	-1.58 ± 0.26 (-1.77 ± 0.30)	-1.12 ± 0.10 (-1.23 ± 0.11)	+2.56 ± 1.03 (+1.65 ± 0.98)	+0.16 ± 0.07 (+0.21 ± 0.13)	+0.11 ± 0.04 (+0.14 ± 0.08)	-0.597 ± 0.077 (-0.389 ± 0.113)	-0.034 ± 0.004 (-0.046 ± 0.013)	-0.025 ± 0.003 (-0.032 ± 0.009)
First year JJA	-27.06 ± 1.19 (-13.09 ± 0.84)	-2.91 ± 0.06 (-3.63 ± 0.17)	-1.13 ± 0.05 (-1.09 ± 0.07)	+6.02 ± 0.49 (+6.36 ± 0.33)	+0.65 ± 0.07 (+1.78 ± 0.15)	+0.25 ± 0.02 (+0.53 ± 0.03)	-0.096 ± 0.087 (+0.356 ± 0.070)	-0.010 ± 0.009 (+0.101 ± 0.023)	-0.004 ± 0.004 (+0.030 ± 0.006)
Years 6-15	-3.01 ± 0.89 (-0.78 ± 0.23)	-1.95 ± 0.19 (-2.40 ± 1.11)	-0.13 ± 0.04 (-0.07 ± 0.02)	-1.92 ± 0.30 (-0.46 ± 0.19)	-2.10 ± 0.87 (-3.42 ± 1.43)	-0.08 ± 0.01 (-0.04 ± 0.02)	-0.619 ± 0.047 (-0.172 ± 0.026)	-0.586 ± 0.163 (-0.919 ± 0.233)	-0.026 ± 0.002 (-0.014 ± 0.002)

176   **Table 1.** Temporal means of the global responses of DSRF (in W m-2), DLRF (in W m-2), and surface temperature (TS; in °C) for
177   BC24 (BC12 in brackets), with the 95% confidence intervals. The confidence intervals for the responses in years 6-16 are computed
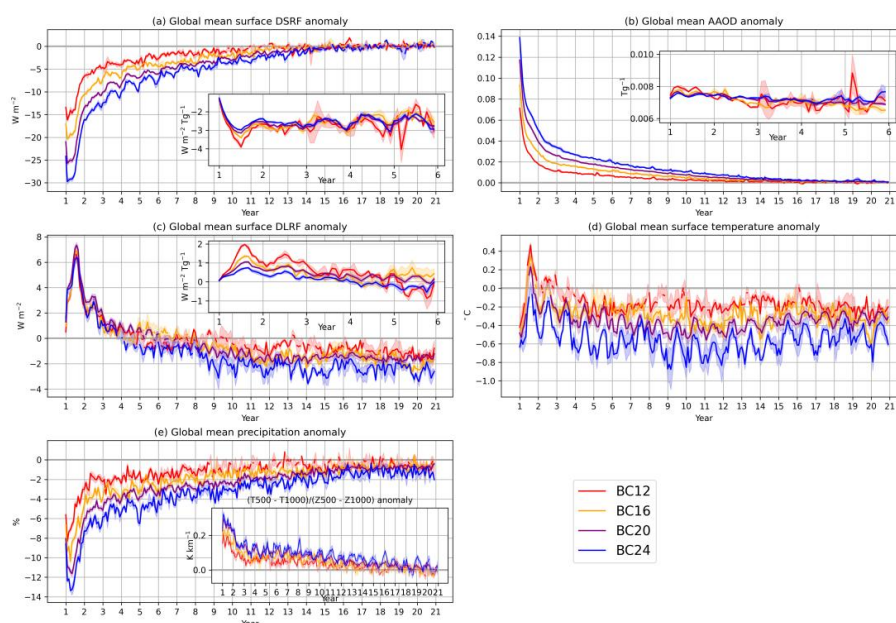178   with lag-1 autocorrelation taken into account, assuming first-order autoaggressive dependence.

179

180
181   **Figure 2.** Monthly averaged global mean responses of (a) surface DSRF, (b) AAOD, (c) surface DLRF, (d) surface temperature,
182   and (e) precipitation. Insets of (a) and (d) are the radiative flux responses divided by the atmospheric BC burden, respectively. Inset
183   of (e) is the monthly averaged global mean responses of the temperature difference between 500 hPa and 1000 hPa, divided by the
184   thickness of the column. Shading indicates the standard error of the mean. Dashed lines indicate where the standard error overlaps
185   with the zero line.

186

187   The global mean aerosol absorption optical depth (AAOD) response is consistent with the surface DSRF response

188   (Fig. 2b), also with an approximately linear scaling (Fig. 2b inset). Unlike the surface DSRF response, the AAOD

189   response starts at its extremum since it depends on the relative radiant flux absorbed by the aerosol rather than the

190   absolute change in the radiative flux. For our best-sampled simulation, BC20, the zonal mean AAOD ranges from 0.1

191   to 0.3 in most of NH in the first simulated year (Fig. 3a). The AAOD becomes comparable between the hemispheres

192   after about 2 simulated years and is reduced to about 0.01-0.02 at high latitudes after 10 years.

193   In addition to the perturbation to shortwave radiative transfer, the longwave radiative transfer would also be perturbed

194   by the aerosol injection due to changes in emissivity and thermal structure of the atmosphere (Ramaswamy & Kiehl,

195   1985). The surface downwelling longwave radiative flux (DLRF) response is initially negligible and then increases as

196   the atmosphere is heated by the BC (Fig. 2c, 3b). For the best-sampled scenario, BC20, the global mean air temperature

197   response exceeds 40 °C at 70 hPa in the first April following the injection and attains a maximum of 45 °C at 70 hPa

198   few months later in June at the beginning of the boreal summer (Fig. 3b). The changes in longwave radiative transfer

199   result in a global mean surface DLRF increase that peaks at +7.33 W m^{-2} in August of the first year (Fig. 2c). The

200   response in surface DLRF in first year JJA is similar among the different scenarios (Fig. 2c, Table 1). This implies that

201   the surface DLRS increase per Tg burden in first year JJA is greater for the weaker forcing scenarios than the stronger

202   forcing scenarios, in contrast to the approximate linearity of surface DSRF response (Fig. 2a,c insets, Table 1). In the

203   long term, the positive response of surface DLRF decays faster than the negative response of surface DSRF (Fig. 2a,c).

204
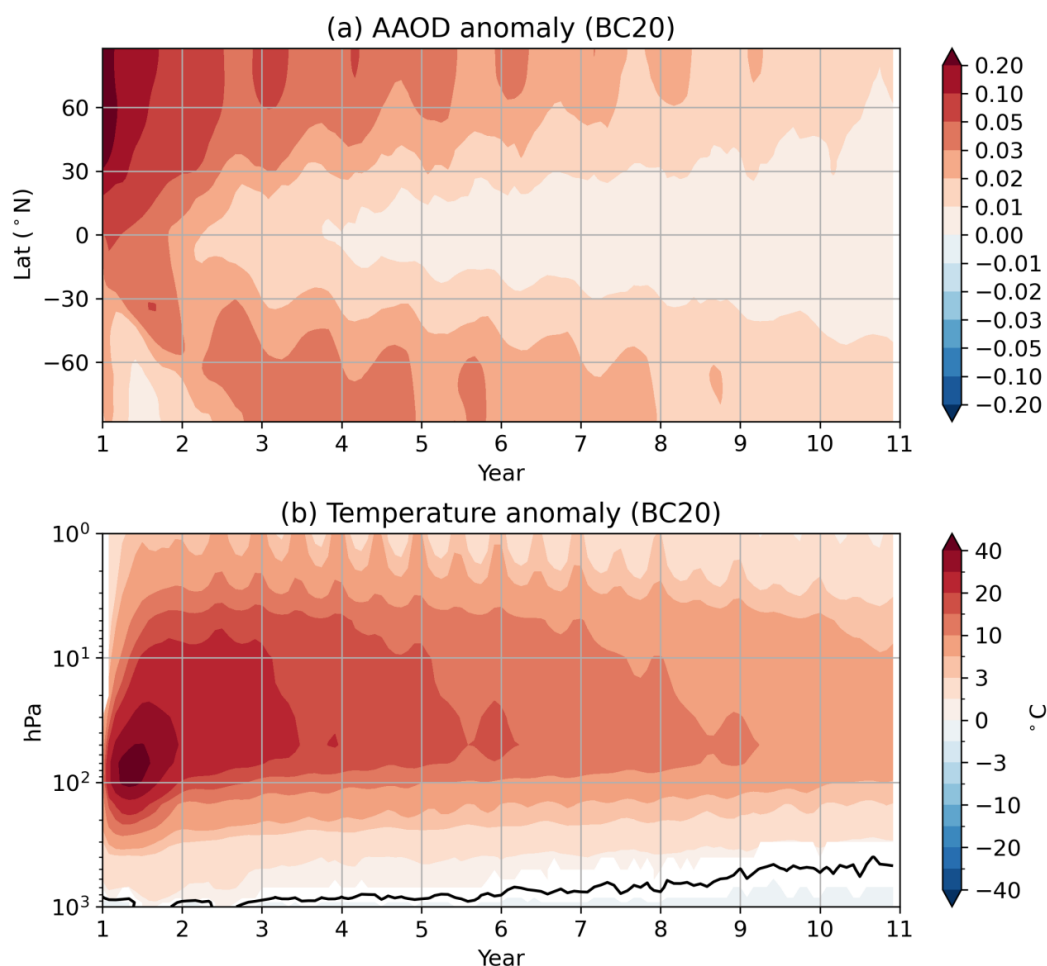
205
206   **Figure 3.** Monthly averaged responses of (a) zonal mean aerosol absorption optical depth at 550 nm and (b) horizontally averaged

207 air temperature. White patches indicate changes that are not significant at 95% confidence level using a t test. In (b), solid black
208 line is the line of 0 K.

209

210 **3.2 Impacts on global temperature and precipitation**

211 The global mean surface temperature is decreased in response to the reduction in surface DSRF, but an unexpected
212 oscillation is seen in the temperature response during the first boreal summer. The reduction in surface DSRF of –
213 14.80 W m^{-2} and –26.96 W m^{-2} causes a rapid global mean surface cooling of –0.389 °C and –0.597 °C in first year
214 JF for BC12 and BC24, respectively (Fig. 2d, Table 1). Surprisingly, instead of a gradual return to the climatological
215 mean, the global mean surface temperature response increases drastically until it reaches a maximum in first year JJA.
216 It is +0.356 °C and –0.096 °C for BC12 and BC24, respectively (Table 1). This implies that the global surface
217 temperature response increases by more than 0.7 °C for BC12 from first year JF to JJA, whereas it increases by 0.5
218 °C for BC24 in the same period. The surface DLRF increase is consistent with the striking transient surface warming.
219 It peaks at +6.36 W m^{-2} and +6.02 W m^{-2} in first year JJA, the same season in which the surface temperature response
220 is at its highest (Fig. 2c,d, Table 1). After the temperature peak in first year JJA, the global mean surface temperature
221 transitions back to a negative response and remains somewhat steady in years 6 to 15 before slowly returning to the
222 climatological mean towards the end of the simulations (Fig. 2d). This is consistent with the trade-off between surface
223 DSRF and DLRF, with the positive response of surface DLRF decaying faster than the negative response of surface
224 DSRF (Fig. 2a,c). In years 6 to 15, the global mean surface temperature responses are –0.172 °C and –0.619 °C for
225 BC12 and BC24 (Table 1). The surface temperature responses per Tg injection are –0.014 °C Tg^{-1} and –0.026 °C Tg^{-1}
226 ^{1}. The nonlinear dependence of surface temperature response on the mass of injection is controlled by the nonlinear
227 dependence of surface DSRF reduction on the mass of injection, -0.07 W m^{-2} Tg^{-1} and –0.13 W m^{-2} Tg^{-1} in years 6 to
228 15. As mentioned above, the stronger early-stage self-lofting effect in the stronger forcing scenarios contributes to the
229 long-term surface DSRF reduction. Thus, the nonlinear self-lofting effect translates to a nonlinear response in the
230 long-term surface temperature response.

231 Despite having surface temperature increase in the first boreal summer, the global mean precipitation response remains
232 negative from the start to near the end of the simulations (Fig. 2e). While reduced precipitation is an expected part of
233 the weakened hydrological cycle associated with nuclear winter (Robock et al., 2007a), the pronounced reduction of
234 precipitation during the period of warming in the first year is consistent with the increase in static stability (Fig. 2e
235 inset). The troposphere is stabilized as the upper troposphere is heated by the light-absorbing BC. This is clear from
236 the best-sampled simulation, BC20 (Fig. 3b). Although the lower tropospheric response is a warming in the first boreal
237 summer, the mid-tropospheric warming is greater. The greater static stability inhibits convection and reduces
238 precipitation. The strongest vertical gradient of temperature response between 100 and 500 hPa emerges in the first
239 year and is weakened afterward, but the sign of the temperature response gradient persists until the end of the simulated
240 period, indicating a more stable troposphere throughout the simulation.

3.3 Spatial pattern of impacts on surface temperature

The regional pattern of surface temperature is forcing-dependent. Comparing the first year JJA responses between BC12 and BC24 reveals stronger polar cooling and larger sea ice expansion under higher forcing (Fig. 4). Moreover, mid-latitude warming is less intense in the higher forcing scenario. Although enhanced mid-tropospheric heating may increase DLRF, the stronger longwave effect under weaker forcing remain uncertain and is examined further below.
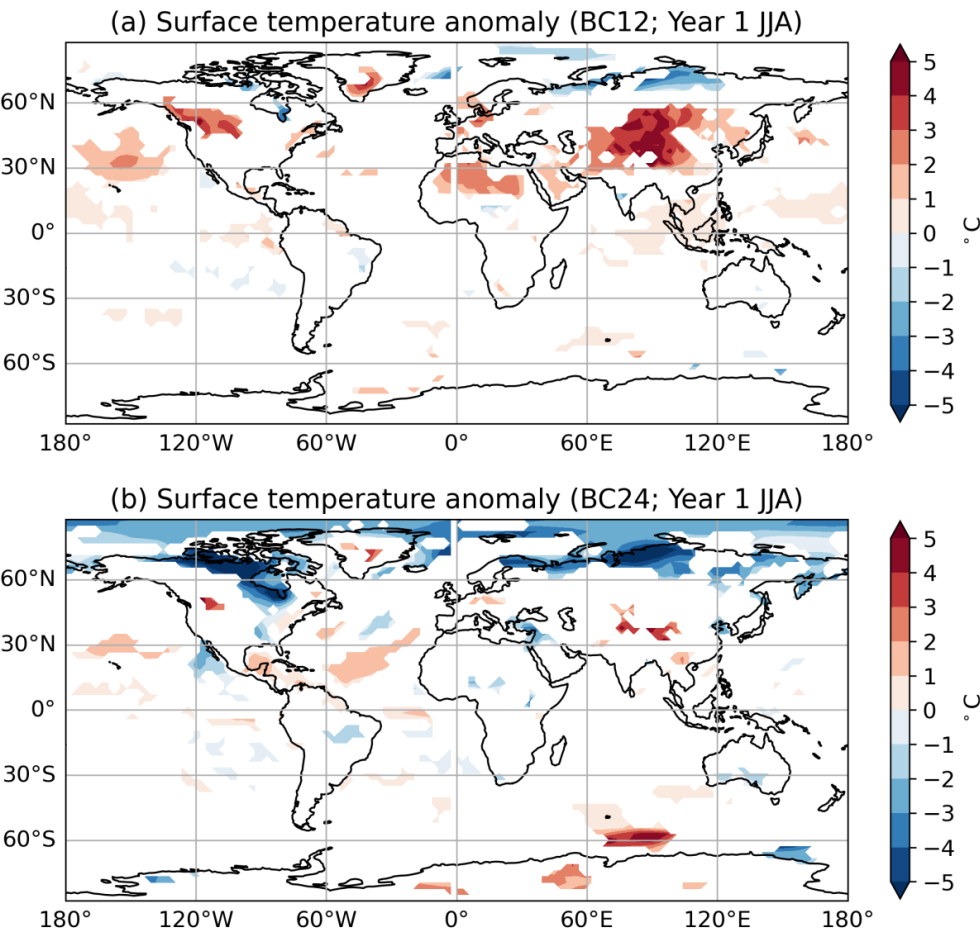
Figure 4. Responses of surface temperature for (a) BC12 and (b) BC24 in JJA of the first simulated year. White patches indicate changes that are not significant at 95% confidence level using a t test. The solid and dashed orange lines indicate the sea ice lines for the scenario and for the climatology, respectively. It is defined as the grids with 15% sea ice area.

252 To characterize this transient evolution from the initial year to subsequent years, we show the best sampled simulation,

253 BC20, contrasting JF and JJA of the first year – marked by the pronounced surface temperature oscillation – with the

254 quasi-steady response over years 6 to 15.

255 In the first two months following the injection, substantial surface cooling is seen on land as a result of the surface

256 DSRF reduction. In NH, there is a statistically significant maximum cooling of about 8 °C in continental regions in

257 the JF-mean (Fig. 5a). The reduction in surface DSRF causes most of the cooling, but the dynamical response likely

258 contributed to some of the temperature responses. For example, the cooling around Greenland and the warming north

259 of Siberia are likely due to a positive Arctic-Oscillation-like (AO) response (Fig. 5a; also see Fig. A1 for the regressed

260 positive AO pattern in the control simulations; Stenchikov et al., 2002). A stronger AO-like response was shown for a

261 5 Tg India-Pakistan case by Robock et al. (2007b). In December to January (DJF) over years 6 to 15, the maximum

262 cooling is at high latitudes, accompanied by sea-ice extent increase (Fig. 5b). This extends to a significant cooling of

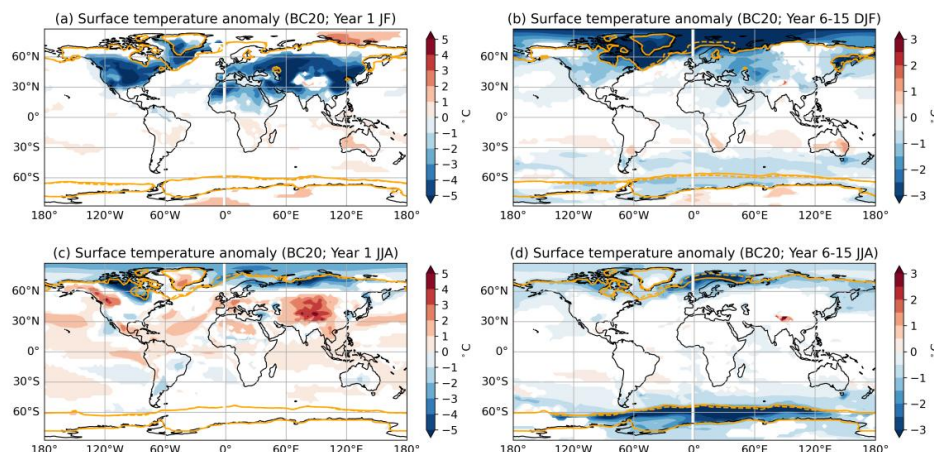263 2-3 °C in Europe and around 1.5 °C in southern Canada and the United States.

264

Figure 5. Responses of surface temperature as in Fig. 4 but for BC20 in (a) JF of the first year, (b) DJF of years 6-15, (c) JJA of the first year, and (d) JJA of years 6-15. White patches indicate changes that are not significant at 95% confidence level using a t test.

269

270 In the first boreal summer following the fire, substantial warming is seen in parts of Africa, North America, Greenland,

271 and Tibet. A warming of up to +3-5 °C develops around Tibet, +2-3 °C in southern Greenland and the western North

272 America, and +1-2 °C in northern Africa (Fig. 5c; and see Fig. 4 for the corresponding plots for BC12 and BC24).

273 These areas are associated with relatively larger surface DLRF response (Fig. 6a). To better understand changes in the

274 surface energy exchange, we calculated the surface net energy imbalance, which takes into account net shortwave

275 radiative flux, net longwave radiative flux, sensible heat flux, and latent heat flux. The surface net energy imbalance

276   is highly localized during the first boreal summer (Fig. 6b). For most land surfaces in NH, the net energy imbalance

277   ranges from +2 to +5 W m^{-2} (a positive sign corresponds to warming). Contributing to this positive response is not

278   only a decrease in surface net longwave radiative flux (defined positive upward), but also a decrease in the turbulent

279   fluxes as the atmospheric stability increases (turbulent fluxes not shown). Although the net energy imbalance is mostly

280   negative for oceanic surface regions, especially at high latitudes, the higher heat capacity of ocean buffers the ocean

281   surface temperature changes. The localized warming on land with adjustment by advection may result in the

282   temperature response pattern and the positive global mean surface temperature response in the first boreal summer

283   (Fig. 2c, 5c, A2). The long-term response for boreal summer shows statistically significant surface cooling mostly at

284   high latitudes (Fig. 5d).

285   Overall, these simulations reveal a whipsaw effect on the surface temperature in the first year, where there is a quick

286   transition from the very cold initial conditions to much warmer conditions over midlatitude land surfaces, and then a

287   transition to strong mid-to-high latitude cooling as sea ice and ocean adjustments kick in.

288
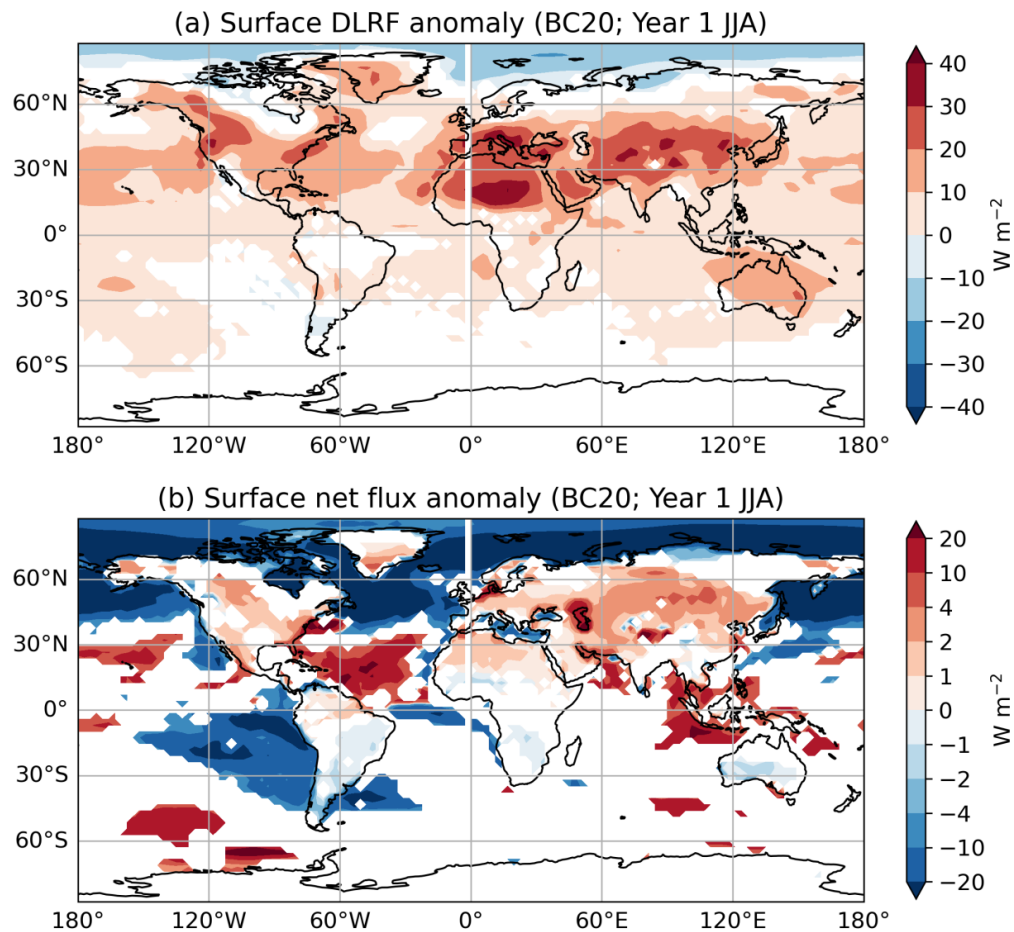
Figure 6. Responses of (a) surface DLRF, and (b) surface net flux in JJA of the first year for BC20. The surface net flux includes net shortwave radiative flux, net longwave radiative flux, latent heat flux, and sensible heat flux. The fluxes are defined as positive downward. White patches indicate changes that are not significant at 95% confidence level using a t test.

4 Discussions and conclusions

In this study, we explore the potential climate impacts of a hypothetical nuclear war between the United States and Russia, using a set of sensitivity studies with different low-to-moderate forcing scenarios using CanESM5. The forcing scenarios range from 12 to 24 Tg of BC injection at UTLS over the United States and Russia. We demonstrate, for the first time, the possibility of a transient global warming response in the first year following fire emissions in low-to-

14

299   moderate forcing nuclear war scenarios. The result highlights the nonlinear nature of the aerosol lifetime and thermal
300   response, which can diverge substantially from those in strong-forcing cases.

301   During the first few months after injection, the global mean surface DSRF is drastically reduced, resulting in
302   substantial global surface cooling, especially over NH land areas. Midway through the first year, however, a sign
303   reversal occurs in the global mean surface temperature response, producing a transient warming before temperature
304   returns to a negative response by year's end. This short-term warming is more pronounced under the weaker forcing
305   scenario, where a larger fraction of BC remains in the lower atmosphere. The enhanced DLRF at the surface, together
306   with reduced cooling via turbulent fluxes, contributed substantially to this warming. This signal is consistent with a
307   stronger nighttime temperature increase (see Fig. A3 for daily minimum surface temperature and daily maximum
308   surface temperature responses during year 1 JJA). The downwelling longwave enhancement likely stems from
309   increased emissivity associated with tropospheric BC burden (Ramaswamy & Kiehl, 1985), although concurrent water
310   vapor changes could also modulate radiative transfer. Further investigation into the sensitivity of the longwave
311   response to the vertical smoke profile and varying water vapor content is warranted for the low-to-moderate forcing
312   scenarios.

313   Absorbing particles above reflective surfaces can induce warming by absorbing shortwave radiation reflected from
314   below and reemitting in the longwave (Bond et al., 2013). This may explain why the warming is mainly confined to
315   dry, high-albedo regions such as Tibet, western North America, and northern Africa (see Fig. A4 for surface albedo in
316   year 1 JJA). Although BC deposition slightly decreased surface albedo in these regions (not shown), the effect was
317   too small to significantly influence DSRF. Moreover, a decreased albedo and greater shortwave absorption could not
318   account for the simulated nighttime warming (Fig. A3; Kleidon & Renner, 2017).

319   The lifetime and transport of BC aerosol are key for understanding the resulting climate effects. In our low-to-moderate
320   forcing scenarios, a larger initial injection led to a greater portion of BC reaching and persisting in the upper
321   atmosphere due to enhanced self-lofting (Stenke et al., 2013). This nonlinear dependence of upper atmospheric burden
322   on the initial injection is critical for the long-term climate response as aerosols in the upper atmosphere have longer
323   lifetime. Hence, both the transient surface warming and the subsequent long-term cooling exhibit nonlinear
324   dependence on injection mass. Our simulations show a faster removal rate compared to the previous studies: over two-
325   thirds of the emitted BC is removed within the first simulated year, whereas other studies reported less than one-third
326   removal for cases with a UTLS injection of 150 Tg over the United States and Russia and of 5 Tg over India and
327   Pakistan (Coupe et al., 2019; Mills et al., 2014; Pausata et al., 2016; Robock et al., 2007b; Wagman et al., 2020). This
328   may reflect the lower concentrations of BC in our 12-24 Tg injections compared to both 150 Tg United States-Russia
329   and 5 Tg India-Pakistan cases. Additionally, model differences – such as aerosol coagulation treatment, gravitational
330   settling, and model-top height – also affect the removal rate (Pausata et al., 2016; Coupe et al., 2019; Robock et al.,
331   2007b). Future research should include systematic model intercomparisons to constrain these uncertainties.

332   The upper atmosphere experiences intense heating the absorbing BC. For BC20, the average temperature response at
333   200 hPa exceeds 15 °C midway through the first year (Fig. 3b). This is comparable to the temperature response at 200
334   hPa in the 150 Tg USA-Russia scenario (Coupe et al., 2019; Robock et al., 2007a). However, unlike those studies, our

335 zero-isotherm remained near the surface in the first few years, (Fig. 3b), likely because their injections were greater

336 and occurred in May, whereas ours began in January. The temperature response at 200 hPa for BC20 also exceeds that

337 in the 5 Tg India-Pakistan case from Mills et al. (2014) and Pausata et al. (2016). Although Mills et al. (2014) have

338 reported that the choice of the initial season did not significantly affect the BC distribution or the climate impact for

339 the 5 Tg India-Pakistan case, this may not be true for our 20 Tg USA-Russia case, which has initially less concentrated

340 BC particles and less insolation in January. Also, for the same 5 Tg India-Pakistan scenario that starts the injection on

341 January 1st, Pausata et al. (2016) found the temperature change to peak at 50 hPa 4 months after the injection in

342 NorESM1-M (model top at 3 hPa), unlike the peak below 1 hPa at the beginning in CESM1-WACCM4 (model top at

343 5.1×10^{-6} hPa) from Mills et al. (2014). This indicates that the heating rate and vertical temperature structure depend

344 strongly on the model configuration as well.

345 The climate effects on temperature and precipitation in our results are linked to impacts that warrant further study. The

346 vertical structure of the warming enhances stability in the troposphere during the entire course of the simulation, which

347 is coherent with the decreased precipitation (Fig. 2e inset). The long-term cooling is mainly confined to high latitudes

348 and is not as drastic as the initial cooling in the midlatitudes. Together persistent cooling and reduced precipitation

349 could still depress agricultural productivity (Xia & Robock, 2013; Xia et al., 2022). Conversely, the first-year transient

350 warming occurs mostly over arid regions that are not major croplands and thus is unlikely to enhance yields. Instead,

351 the warmer and drier surface conditions could heighten wildfire risk (Byrne et al., 2024).

352 OC is also a possible constituent of the smoke apart from BC. While OC is more short-lived and less absorbing in the

353 visible range (Forrister et al., 2015), recent studies show that including OC can enhance surface cooling and

354 stratospheric heating but reduce aerosol residence time by promoting coagulation (Pausata et al., 2016). We did not

355 include OC emission in our scenarios, as our version of CanESM5.1 lacks coagulation processes. For further work,

356 we will address this limitation using an updated version of CanESM with the Piecewise log-normal Aerosol Model

357 (PAM; von Salzen, 2006), which allows for a more complete treatment of aerosol microphysics.

358 In summary, our simulations demonstrate, for the first time, the possibility of a transient global warming signal during

359 the first year following fire emissions in low-to-moderate forcing nuclear war scenarios. This finding stands in contrast

360 to the uniformly cooling response typically associated with strong-forcing nuclear winter events. The result highlights

361 the nonlinear nature of the aerosol lifetime and thermal response, which can diverge substantially from those in strong-

362 forcing cases. The warming arises from a complex balance between surface shortwave, longwave, and turbulent fluxes.

363 While this longwave-driven warming is likely overwhelmed by surface shortwave reduction as the forcing increases

364 and more BC aerosol is lofted into the stratosphere, its emergence here underscores the importance of model

365 representations of aerosol microphysics and feedbacks involving turbulent heat exchange. The transient and spatially

366 heterogeneous surface warming revealed in our simulations merits attention for its potential societal and

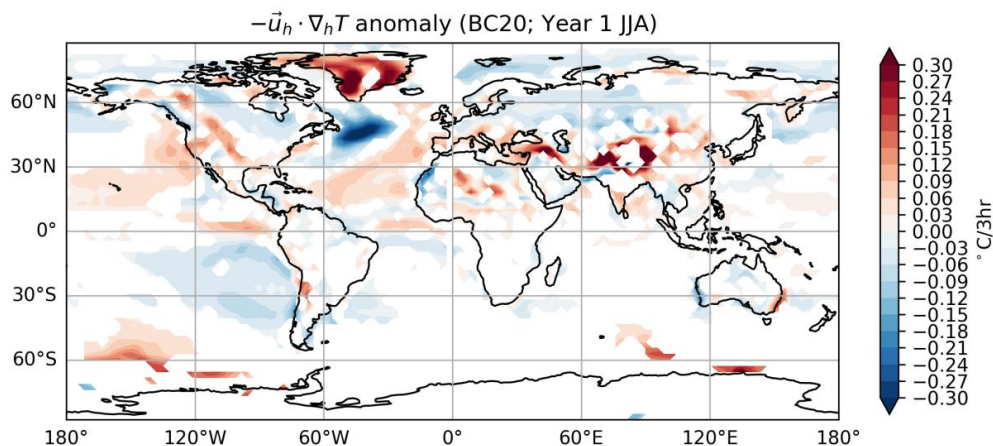367 environmental implications, even under relatively modest nuclear exchange scenarios.

368 **Appendix A**

369
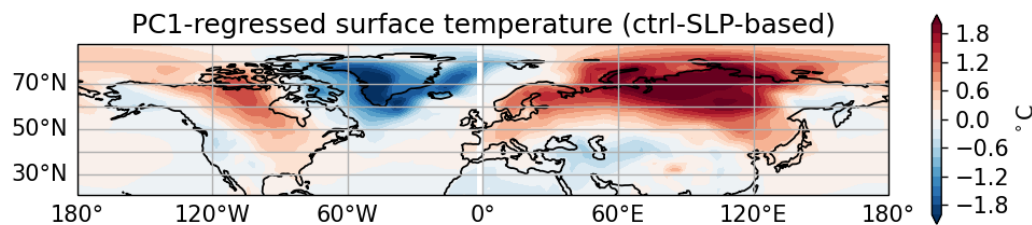
370
371 **Figure A1.** The positive AO pattern in the control simulations, obtained by regressing surface temperature onto the first principal
372 component (PC1) of sea-level pressure (SLP). 20°N-90°N daily zonal-mean SLP anomalies in DJF were used.
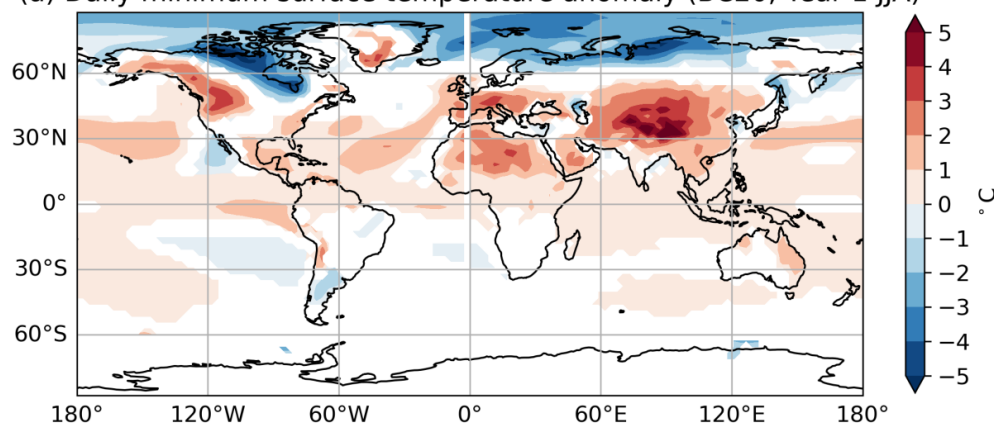
373

374
375 **Figure A2.** Temperature advection responses in JJA of the first year for BC20. The sign is defined such that positive values imply
376 a positive local temperature tendency due to temperature advection. White patches indicate changes that are not significant at 95%
377 confidence level using a t test.

378

Figure A3. Responses of (a) daily minimum and (b) daily maximum surface temperature in JJA of the first year for BC20. White patches indicate changes that are not significant at 95% confidence level using a t test.
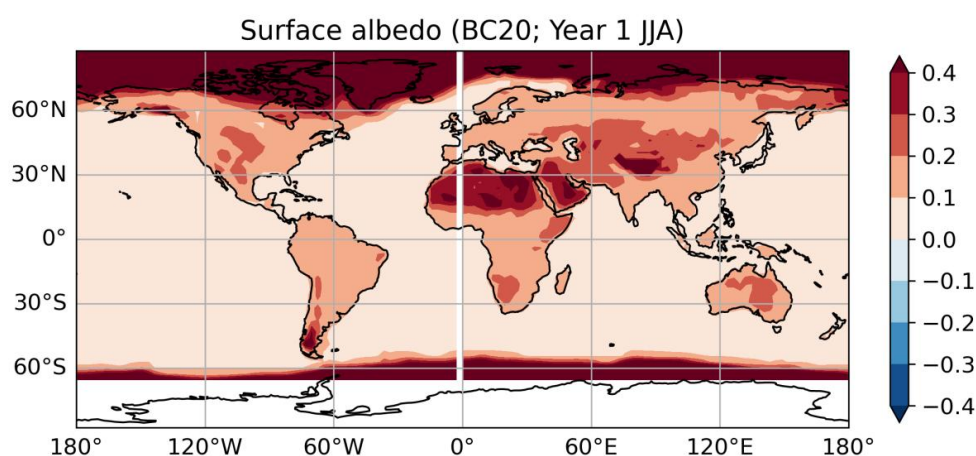
Surface albedo (BC20; Year 1 JJA)

Figure A4. Surface albedo in JJA of the first year for BC20.

Code and data availability

Both CanESM and the related tool imsi are released under the Open Government Licence Canada – 2.0. This license permits anyone to use or adapt them for lawful purposes, including commercial use, provided appropriate acknowledgement is given. Postprocessed output from the CanESM simulations, needed to reproduce the main figures, are publicly available on the University of Toronto Dataverse at https://doi.org/10.5683/SP3/UG2598. The full model outputs from the simulations are large and stored on the Trillium supercomputer at the SciNet HPC Consortium. Additional data from these simulations can be provided upon request by contacting Anson Cheung or Paul Kushner.

Author contributions

PJK and FSRP coordinated the project and acquired financial support for the project; PJK and AKHC designed the simulations; AKHC adapted CanESM code and performed the simulations; AKHC analyzed the model output with contributions from all co-authors; AKHC wrote the manuscript draft; PJK, FSRP, ZZ, and MB reviewed and edited the manuscript.

Competing interests

The authors declare that they have no conflict of interest.

References

Bardeen, C. G., Kinnison, D. E., Toon, O. B., Mills, M. J., Vitt, F., Xia, L., Jägermeyr, J., Lovenduski, N. S., Scherrer, K. J. N., Clyne, M., and Robock, A.: Extreme ozone loss following nuclear war results in enhanced surface ultraviolet radiation, Journal of Geophysical Research: Atmospheres, 126(18), https://doi.org/10.1029/2021JD035079, 2021.

Bond, T. C., Doherty, S. J., Fahey, D. W., Forster, P. M., Berntsen, T., DeAngelo, B. J., Flanner, M. G., Ghan, S., Kärcher, B., Koch, D., Kinne, S., Kondo, Y., Quinn, P. K., Sarofim, M. C., Schultz, M. G., Schulz, M., Venkataraman, C., Zhang, H., Zhang, S., Bellouin, N., Guttikunda, S. K., Hopke, P. K., Jacobson, M. Z., Kaiser, J. W., Klimont, Z., Lohmann, U., Schwarz, J. P., Shindell, D., Storelvmo, T., Warren, S. G., and Zender, C. S.: Bounding the role of black carbon in the climate system: A scientific assessment. J. Geophys, Res. Atmos., 118, 5380-5552, doi:10.1002/jgrd.50171, 2013.

Byrne, B., Liu, J., Bowman, K. W., Pascolini-Campbell, M., Chatterjee, A., Pandey, S., Miyazaki, K., van der Werf, G. R., Wunch, D., Wennberg, P. O., Roehl, C. M., and Sinha, S.: Carbon emissions from the 2023 Canadian wildfires, Nature 633, 835-839, https://doi.org/10.1038/s41586-024-07878-z, 2024.

Cole, J. N. S., von Salzen, K., Li, J., Scinocca, J., Plummer, D., Arora, V., McFarlane, N., Lazare, M., MacKay, M., and Verseghy, D.: The Canadian Atmospheric Model version 5 (CanAM5.0.3), Geosci. Model Dev., 16, 5427-5448, https://doi.org/10.5194/gmd-16-5427-2023, 2023.

Coupe, J., Bardeen, C. G., Robock, A., and Toon, O. B.: Nuclear Winter Responses to Nuclear War Between the United States and Russia in the Whole Atmosphere Community Climate Model Version 4 and the Goddard Institute for Space Studies ModelE, Journal of Geophysical Research, Atmospheres, 124(15), 8522-8543. https://doi.org/10.1029/2019JD030509, 2019.

Croft, B., Lohmann, U., and von Salzen, K.: Black carbon ageing in the Canadian Centre for Climate modelling and analysis atmospheric general circulation model, Atmospheric Chemistry and Physics, 5, 1931-1949, 2005.

Dai, Y., Hitchcock, P., and Simpson, I. R.: What Drives the Spread and Bias in the Surface Impact of Sudden Stratospheric Warmings in CMIP6 Models? J. Climate, 37, 3917-3942, https://doi.org/10.1175/JCLI-D-23-0622.1, 2024.

434   Eyring, V., Bony, S., Meehl, G. A., Senior, C. A., Stevens, B., Stouffer, R. J., and Taylor, K. E.: Overview of the
435   Coupled Model Intercomparison Project Phase 6 (CMIP6) experimental design and organization. Geoscientific Model
436   Development, 9(5), 1937-1958, https://doi.org/10.5194/gmd-9-1937-2016, 2016.

437   Forrister, H., Liu, J., Scheuer, E., Dibb, J., Ziemba, L., Thornhill, K. L., Anderson, B., Diskin, G., Perring, A. E.,
438   Schwarz, J. P., Campuzano-Jost, P., Day, D. A., Palm, B. B., Jimenez, J. L., Nenes, A., and Weber, R. J.: Evolution of
439   brown carbon in wildfire plumes, Geophys. Res. Lett., 42, 4623–4630, doi: 10.1002/2015GL063897, 2015.

440   Gettelman, A., Mills, M. J., Kinnison, D. E., Garcia, R. R., Smith, A. K., Marsh, D. R., Tilmes, S., Vitt, F., Bardeen,
441   C. G., McInerny, J., Liu, H.-L., Solomon, S. C., Polvani, L. M., Emmons, L. K., Lamarque, J.-F., Richter, J. H.,
442   Glanville, A. S., Bacmeister, J. T., Phillips, A. S., Neale, R. B., Simpson, I. R., DuVivier, A. K., Hodzic, A., and Randel,
443   W. J.: The whole atmosphere community climate model version 6 (WACCM6), Journal of Geophysical Research:
444   Atmospheres, 124(23), 12380-12403, https://doi.org/10.1029/2019JD030943, 2019.

445   Ghan, S. J., Smith, S. J., Wang, M., Zhang, K., Pringle, K., Carslaw, K., Pierce, J., Bauer, S., and Adams, P.: A simple
446   model of global aerosol indirect effects, Journal of Geophysical Research. Atmospheres, 118(12), 6688-6707,
447   https://doi.org/10.1002/jgrd.50567, 2013.

448   Glasstone, S., Dolan, P. J., United States. Department of Defense, United States Department of Energy, and United
449   States Defense Atomic Support Agency.: The effects of nuclear weapons (3rd ed.), U.S. Dept. of Defense, 1977.

450   Holton, J. R., Haynes, P. R., McIntyre, M. E., and Douglass, A. R.: Stratosphere-troposphere exchange, Rev. Geophys.,
451   33, 403-439, https://doi.org/10.1029/95RG02097, 1995.

452   Johnson, B. T. and Haywood, J. M.: Assessing the impact of self-lofting on increasing the altitude of black carbon in
453   a global climate model, Journal of Geophysical Research: Atmospheres, 128, https://doi.org/10.1029/2022JD038039,
454   2023.

455   Kleidon, A. and Renner, M.: An explanation for the different climate sensitivities of land and ocean surfaces based on
456   the diurnal cycle, Earth System Dynamics, 8(3), 849-864, https://doi.org/10.5194/esd-8-849-2017, 2017.

457   Li, J., von Salzen, K., Peng, Y., Zhang, H., and Liang, X.: Evaluation of black carbon semidirect radiative effect in a
458   climate model, Journal of Geophysical Research. Atmospheres, 118(10), 4715-4728,
459   https://doi.org/10.1002/jgrd.50327, 2013.

460   Lohmann, U., von Salzen, K., McFarlane, N., Leighton, H. G., and Feichter, J.: Tropospheric sulfur cycle in the
461   Canadian general circulation model, J. Geophys. Res., 104(D21), 26833-26858, doi:10.1029/1999JD900343, 1999.

462   Lucas, K. A., Orient J. M., Robinson A., Maccabee H., Morris P., Looney G., and Klinghoffer M.: Efficacy of bomb
463   shelters: with lessons from the Hamburg firestorm, South Med J., 83(7), 812-820, doi: 10.1097/00007611-199007000-
464   00022, 1990.

465   Madec, G. and the NEMO team: NEMO ocean engine, version 3.4, Institut Pierre-Simon Laplace Note du Pole de
466   Modélisation 27, 367 pp, 2012.

467   Malone, R. C., Auer, L., Glatzmaier, G., Wood, M., and Toon, O. B.: Influence of solar heating and precipitation
468   scavenging on the simulated lifetime of post-nuclear war smoke, Science, 230(4723), 317-319,
469   https://doi.org/10.1126/science.230.4723.317, 1985.

470 Mills, M. J., Toon, O. B., Lee-Taylor, J., and Robock, A.: Multidecadal global cooling and unprecedented ozone loss
471 following a regional nuclear conflict, Earth's Future, 2(4), 161-176, https://doi.org/10.1002/2013EF000205, 2014.

472 Mills, M. J., Toon, O. B., Turco, R. P., Kinnison, D. E., and Garcia, R. R.: Massive global ozone loss predicted
473 following regional nuclear conflict, Proceedings of the National Academy of Sciences - PNAS, 105(14), 5307-5312,
474 https://doi.org/10.1073/pnas.0710058105, 2008.

475 Namazi, M., von Salzen, K., and Cole, J. N. S.: Simulation of black carbon in snow and its climate impact in the
476 Canadian Global Climate Model, Atmos. Chem. Phys., 15, 10887-10904, https://doi.org/10.5194/acp-15-10887-2015,
477 2015.

478 National Academies of Sciences, Engineering, and Medicine: Potential Environmental Effects of Nuclear War,
479 Washington, DC: The National Academies Press, https://doi.org/10.17226/27515, 2025.

480 Ohneiser, K., Ansmann, A., Witthuhn, J., Deneke, H., Chudnovsky, A., Walter, G., and Senf, F.: Self-lofting of wildfire
481 smoke in the troposphere and stratosphere: simulations and space lidar observations. Atmos. Chem. Phys., 23(4),
482 2901-2925, https://doi.org/10.5194/acp-23-2901-2023, 2023.

483 Pausata, F. S. R., Lindvall, J., Ekman, A. M. L., and Svensson, G.: Climate effects of a hypothetical regional nuclear
484 war: Sensitivity   to   emission   duration   and   particle   composition,   Earth's   Future,   4(11),   498-511,
485 https://doi.org/10.1002/2016EF000415, 2016.

486 Ramaswamy, V. and Kiehl, J. T.: Sensitivities of the radiative forcing due to large loadings of smoke and dust aerosols,
487 J. Geophys. Res., 90(D3), 5597-5613, doi:10.1029/JD090iD03p05597, 1985.

488 Robock, A., Oman, L., and Stenchikov, G. L.: Nuclear winter revisited with a modern climate model and current
489 nuclear arsenals: Still catastrophic consequences, Journal of Geophysical Research - Atmospheres, 112(D13),
490 D13107-n/a, https://doi.org/10.1029/2006JD008235, 2007.

491 Robock, A., Oman, L., Stenchikov, G. L., Toon, O. B., Bardeen, C., and Turco, R. P.: Climatic consequences of
492 regional nuclear conflicts, Atmospheric Chemistry and Physics, 7(8), 2003-2012, https://doi.org/10.5194/acp-7-2003-
493 2007, 2007.

494 Samset, B. H., Wilcox, L. J., Allen, R. J., Stjern, C. W., Lund, M. T., Ahmadi, S., Ekman, A., Elling, M. T., Fraser-
495 Leach, L., Griffiths, P., Keeble, J., Koshiro, T., Kushner, P., Lewinschal, A., Makkonen, R., Merikanto, J., Nabat, P.,
496 Narazenko, L., O'Donnell, D., Oshima, N., Rumbold, S. T., Takemura, T., Tsigaridis, K., and Westervelt, D. M.: East
497 Asian aerosol cleanup has likely contributed to the recent acceleration in global warming, Commun Earth Environ,
498 6543, https://doi.org/10.1038/s43247-025-02527-3, 2025.

499 Scinocca, J. F., McFarlane, N. A., Lazare, M., Li, J., and Plummer, D.: Technical Note: The CCCma third generation
500 AGCM and its extension into the middle atmosphere, Atmos. Chem. Phys., 8, 7055-7074, https://doi.org/10.5194/acp-
501 8-7055-2008, 2008.

502 Shemwell, B. E. and Levendis, Y. A.: Particulates Generated from Combustion of Polymers (Plastics), Journal of the
503 Air & Waste Management Association, 50(1), 94-102, https://doi.org/10.1080/10473289.2000.10463994, 2000.

504 Solomon, F. and Marston, R. Q.: The Medical Implications of Nuclear War, National Academy Press, 1986.

505 Stenchikov, G., Robock, A., Ramaswamy, V., Schwarzkopf, M. D., Hamilton, K., and Ramachandran, S.: Arctic
506 Oscillation response to the 1991 Mount Pinatubo eruption: Effects of volcanic aerosols and ozone depletion, J.
507 Geophys. Res., 107(D24), 4803, doi:10.1029/2002JD002090, 2002.

508 Stenke, A., Hoyle, C. R., Luo, B., Rozanov, E., Gröbner, J., Maag, L., Brönnimann, S., and Peter, T.: Climate and
509 chemistry effects of a regional scale nuclear conflict, Atmospheric Chemistry and Physics, 13(19), 9713-9729,
510 https://doi.org/10.5194/acp-13-9713-2013, 2013.

511 Swart, N. C., Cole, J. N. S., Kharin, V. V., Lazare, M., Scinocca, J. F., Gillett, N. P., Anstey, J., Arora, V., Christian, J.
512 R., Hanna, S., Jiao, Y., Lee, W. G., Majaess, F., Saenko, O. A., Seiler, C., Seinen, C., Shao, A., Sigmond, M., Solheim,
513 L., von Salzen, K., Yang, D., and Winter, B.: The Canadian Earth System Model version 5 (CanESM5.0.3), Geosci.
514 Model Dev., 12, 4823-4873, https://doi.org/10.5194/gmd-12-4823-2019, 2019.

515 Tarshish, N. and Romps, D. M.: Latent heating is required for firestorm plumes to reach the stratosphere, Journal of
516 Geophysical Research: Atmospheres, 127, https://doi.org/10.1029/2022JD036667, 2022.

517 Tewarson, A.: Chapter 4 Generation of Heat and Chemical Compounds in Fires, In P. J. DiNenno (Eds.), SFPE
518 Handbook of Fire Protection Engineering (3rd ed., pp. 3-82--3-161), National Fire Protection Assoc, Inc. Quincy,
519 Mass, 2002.

520 Toon, O. B., Turco, R. P., Robock, A., Bardeen, C., Oman, L., and Stenchikov, G. L.: Atmospheric effects and societal
521 consequences of regional scale nuclear conflicts and acts of individual nuclear terrorism, Atmospheric Chemistry and
522 Physics, 7(8), 1973-2002, https://doi.org/10.5194/acp-7-1973-2007, 2007.

523 Turco, R. P., Toon, O. B., Ackerman, T. P., Pollack, J. B., and Sagan, C.: Climate and Smoke: An Appraisal of Nuclear
524 Winter, Science, 247(4939), 166-176, https://doi.org/10.1126/science.11538069, 1990.

525 von Salzen, K.: Piecewise log-normal approximation of size distributions for aerosol modelling, Atmospheric
526 Chemistry and Physics, 6(5), 1351-1372, https://doi.org/10.5194/acp-6-1351-2006, 2006.

527 von Salzen, K., Scinocca, J. F., McFarlane, N. A., Li, J., Cole, J. N. S., Plummer, D., Verseghy, D., Reader, M. C., Ma,
528 X., Lazare, M., and Solheim, L.: The Canadian Fourth Generation Atmospheric Global Climate Model (CanAM4).
529 Part I: Representation of Physical Processes, Atmosphere-Ocean, 51(1), 104-125,
530 https://doi.org/10.1080/07055900.2012.755610, 2013.

531 Wagman, B. M., Lundquist, K. A., Tang, Q., Glascoe, L. G., and Bader, D. C.: Examining the climate effects of a
532 regional nuclear weapons exchange using a multiscale atmospheric modeling approach, Journal of Geophysical
533 Research: Atmospheres, 125, https://doi.org/10.1029/2020JD033056, 2020.

534 Wood, R.: Drizzle in Stratiform Boundary Layer Clouds. Part II: Microphysical Aspects, Journal of the Atmospheric
535 Sciences, 62(9), 3034-3050, https://doi.org/10.1175/JAS3530.1, 2005.

536 Wu, K., Li, J., von Salzen, K., and Zhang, F.: Explicit solutions to the mixing rules with three-component inclusions,
537 Journal of Quantitative Spectroscopy & Radiative Transfer, 207, 78-82, https://doi.org/10.1016/j.jqsrt.2017.12.020,
538 2018.

539 Xia, L. and Robock, A: Impacts of a nuclear war in South Asia on rice production in Mainland China, Climatic Change,
540 116, 357-372, https://doi.org/10.1007/s10584-012-0475-8, 2013.

541 Xia, L., Robock, A., Mills, M., Stenke, A. and Helfand, I.: Decadal reduction of Chinese agriculture after a regional

542 nuclear war, Earth's Future, 3(2), 37-48, https://doi.org/10.1002/2014EF000283, 2015.

543 Xia, L., Robock, A., Scherrer, K., Harrison, C. S., Bodirsky, B. L., Weindl, I., Jägermeyr, J., Bardeen, C. G., Toon, O.

544 B., and Heneghan, R.: Global food insecurity and famine from reduced crop, marine fishery and livestock production

545 due to climate disruption from nuclear war soot injection, Nat Food, 3, 586–596, https://doi.org/10.1038/s43016-022-

546 00573-0, 2022.

547 Yu, P., Davis, S. M., Toon, O. B., Portmann, R. W., Bardeen, C. G., Barnes, J. E., Telg, H., Maloney, C., and Rosenlof,

548 K. H.: Persistent Stratospheric Warming Due to 2019-2020 Australian Wildfire Smoke, Geophysical Research Letters,

549 48(7), https://doi.org/10.1029/2021GL092609, 2021.

550 Zanchettin, D., Khodri, M., Timmreck, C., Toohey, M., Schmidt, A., Gerber, E., Hegerl, G., Robock, A., Pausata, F.,

551 Ball, W., Bauer, S., Bekki, S., Dhomse, S., LeGrande, A., Mann, G., Marshall, L., Mills, M., Marchand, M., Niemeier,

552 U., Poulain, V., Rozanov, E., Rubino, A., Stenke, A., Tsigaridis, K., and Tummon, F.: The Model Intercomparison

553 Project on the climatic response to Volcanic forcing (VolMIP): experimental design and forcing input data for CMIP6,

554 Geosci. Model Dev., 9, 2701-2719, https://doi.org/10.5194/gmd-9-2701-2016, 2016.